Doped graphene characterized via Raman spectroscopy and magneto-transport measurements

Marie-Luise Braatz[1,2], Nils-Eike Weber[3,+], Barthi Singh[4,5], Klaus Müllen[4], Xinliang Feng[4*], Mathias Kläui[1#] and Martin Gradhand[1,6]

[1]Institute of Physics, Johannes Gutenberg University Mainz, Staudingerweg 7, 55128 Mainz, Germany

[2]Graduate School of Excellence Materials Science in Mainz, Staudingerweg 9, 55128 Mainz, Germany

[3]Carbon Materials Innovation Center (CMIC), BASF SE, 67056 Ludwigshafen, Germany

[4]Max Planck Institute for Polymer Research, Ackermannweg 10, 55128 Mainz, Germany

[5]Department of Applied Physics, Delhi Technological University, Delhi, 110042, India

[6]H. H. Wills Physics Laboratory, University of Bristol, Tyndall Ave, BS8-1TL, United Kingdom

Corresponding author: klaeui@uni-mainz.de

+ Present address: Scienta Omicron GmbH, Limburger Strasse 75, 65232 Taunusstein, Germany

* Present address: Max Planck Institute of Microstructure Physics, Weinberg 2, 06120 Halle, Germany

Abstract

Functionalizing graphene beyond its intrinsic properties has been a key concept since the first successful realization of this archetype monolayer system. While various concepts, such as doping, co-doping and layered device design, have been proposed, the often complex structural and electronic changes are often jeopardizing simple functionalization attempts. Here, we present a thorough analysis of the structural and electronic properties of co-doped graphene via Raman spectroscopy as well as magneto-transport and Hall measurements. The results highlight the challenges in understanding its microscopic

properties beyond the simple preparation of such devices. It is discussed how co-doping with N and B dopants leads to effective charge neutral defects acting as short-range scatterers, while charged defects introduce more long-range scattering centers. Such distinct behavior may obscure or alter desired structural as well as electronic properties not anticipated initially. Exploring further the preparation of effective pn-junctions, we highlight step by step how the preparation process may lead to alterations in the intrinsic properties of the individual layers. Importantly, it is highlighted in all steps how the inhomogeneities across individual graphene sheets may challenge simple interpretations of individual measurements.

Introduction

Chemical doping of graphene is widely used to modify the properties of graphene [1] adapting it to a wide set of applications from biosensing to batteries or catalysis [2–4]. Among the most commonly used dopants are nitrogen and boron [5], where the induced lattice distortion is relatively small [6]. The combination of both dopants in one sample has been proposed for supercapacitors [7] or biological applications [8]. Including further dopants such as the combination of nitrogen and sulfur [9,10] or boron and beryllium [11], an even larger variety of tuning properties is possible. While several proposals have been made, not many details are established about the characterization of the electronic structure and material properties of such co-doped samples. Furthermore, combining graphene layers with different dopants and doping levels opens an even wider range of combinations and thus property tuning, which is just starting to be explored.

Here, we present investigations on selected samples with different doping levels including co-doping to establish a clearer picture of the induced changes of the underlying graphene transport properties. To investigate the effect of different types of dopants on the physical properties of graphene, co-doped samples of nitrogen and boron are compared to only nitrogen-doped graphene. By using complementary

optical and electronic measurement techniques, different properties such as structural order, electronic mobility as well as the transport relaxation times of the samples are ascertained.

Furthermore, we combine two differently doped layers into a heterostructure. This allows us to explore the possible creation of junctions based on graphene sheets with different doping levels.

Methods

The nitrogen-doped (sample A and B) as well as the boron and nitrogen co-doped samples were grown by chemical vapor deposition (CVD) on copper [12]. The dopants were incorporated by adding different precursors during the growth phase: varying amounts of NH_3 for the N-doped and the in-house synthesized organic precursor (B_2N_2 Dibenzo[a,e]pentalenes ($C_{30}H_{30}B_2N_2$)) BNNB-DBP for the B,N-co-doped sample. The transfer of the graphene from copper to Si/SiO_2 (p-doped Si covered with 300 nm SiO_2) followed a standard wet transfer protocol [13]. First, the graphene was covered with polymethyl-methacrylate (PMMA), then the copper was etched by ammonium persulfate (3%). Next, the samples were placed on water for cleaning and finally transferred to the Si/SiO_2 substrate. For the double transfer, a second graphene sheet was deposited on top of the first one by using the same procedure. A sketch of this configuration can be found in the corresponding section in Fig. 5a. For both types of transfer, the graphene pieces were approximately square with an edge length between 0.5 and 1 cm. Raman spectroscopy was performed at a wavelength of 532 nm. For the subsequent electronic measurements the samples were contacted with silverpaste in a four-probe geometry. An additional contact was placed on the backside to allow for electrical gating of the samples. The measurements were performed in a helium cryostat in vacuum at temperatures down to 3K and magnetic fields up to 8T applied perpendicular to the sample surface. Furthermore, on sample A, transmission electron microscopy (TEM) and x-ray photoelectron spectroscopy (XPS) were performed. Details on the experimental methods can be found in the supplementary information.

Results and Discussion

B and N co-doped samples

Raman spectroscopy was used to characterize the structure of the samples. In all cases the characteristic graphene peaks, 2D (~2679 cm^{-1} at 532nm) and G (~1580 cm^{-1} at 532nm), can be observed. In addition, the D peak (~1350 cm^{-1} at 532nm), which is only present for imperfect graphene [14,15], can be clearly identified (see inset Fig. 1(a)). The symmetric, single-peak, shape of the 2D-peak and the intensity ratio of

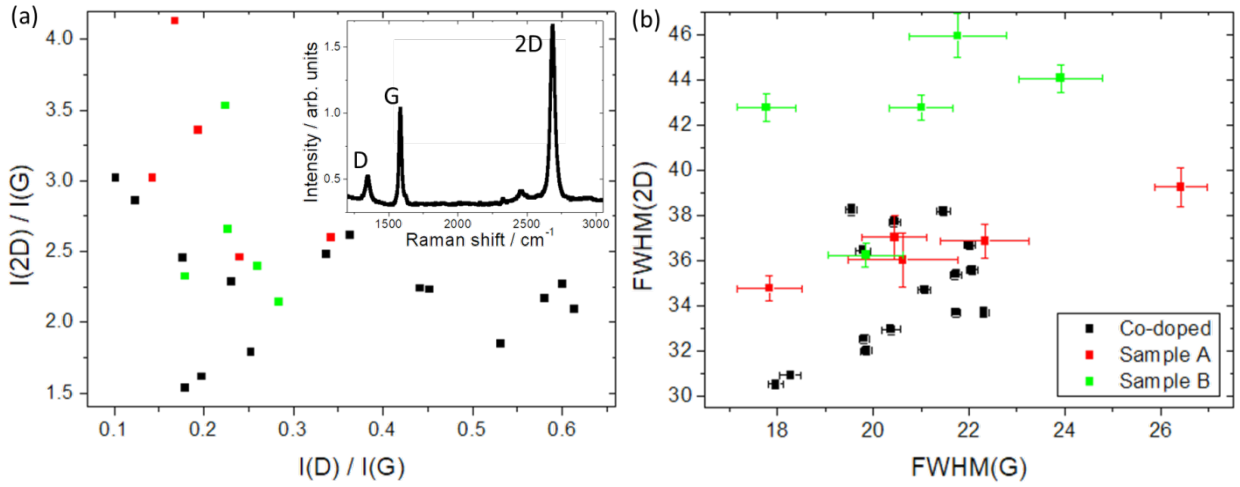

Figure 1: The Raman spectroscopy for all graphene samples with the N doped samples A (red) and B (green) and the Co-doped sample (black). a) Ratio of 2D to G peak intensity vs. the ratio of the D to the G peak with an inset of the Raman spectrum for the co-doped sample. b) The FWHM of the 2D peak vs. the FWHM of the G peak for all three samples.

the 2D- and G-peak, equal or larger than 2 (Fig. 1a), identify our samples as monolayer graphene with a reasonably low level of defect concentrations [16,17]. To confirm the monolayer nature of the samples, TEM was performed on sample A. The image in Fig. 2 shows an area of polycrystalline graphene with the grain boundary indicated by the red arrows. As has been shown before [18] the ratio of the intensities of 2D and G peak I(2D)/I(G) is generally taken to be a good measure of the defect concentration. For relatively pure graphene I(G) changes weakly while the intensity of the 2D peak becomes gradually lower with higher defect concentration. While this ratio is on average lower for the co-doped sample, the spread suggests

significant inhomogeneities across the sample. However, the considerably larger values for the I(D)/I(G) ratio in the co-doped graphene points to a larger defect concentration at least on average for this system. Nevertheless, the scenario for the I(D)/I(G) is slightly more complicated as discussed previously [19]. Due to competing mechanisms this peak intensity will increase proportionally with the defect concentration but will decrease again beyond a certain threshold [20]. This behavior makes it difficult to identify the defect concentration solely by the I(D) intensity.

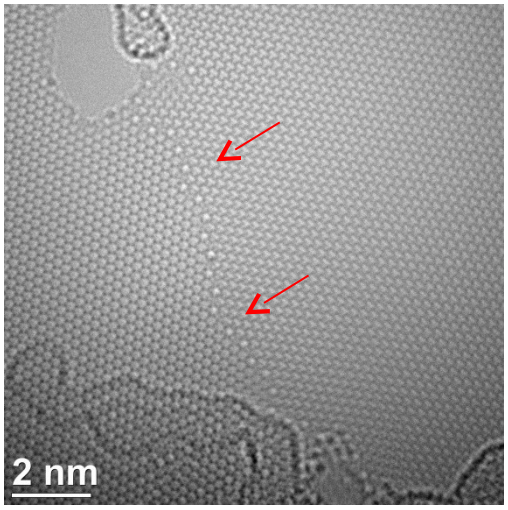

Figure 2: TEM image of sample A showing a grain boundary in monolayer graphene

In Fig. 1b we summarize the results for the full width at half maximum (FWHM) of the 2D as well as the G resonances. It is well established that the FWHM(G) will increase with increasing defect level, but the precise quantitative change will depend on the nature of the defect [21]. Any drastic increase of the FWHM of the 2D-peak would be associated with n-layer graphene but the maximal values observed here are substantially below any indication of multilayer graphene[17] and clearly identifies the systems as monolayer graphene. As for the intensities, the data is not conclusive and underlines the significant inhomogeneities across even individual samples. For any practical application this becomes a challenge as the properties might change rapidly across individual samples over reasonably short scales (probed by the spot of the laser in the Raman spectroscopy).

Finally, it is important to note the strong dependence of the intensities as well as the FWHM on the charge carrier concentration. Generally, the G resonances stiffen away from the Dirac point while the intensities of the D peak increase at the Dirac point [19]. This makes it difficult to draw direct conclusions from the Raman data as the different defect levels will change the scattering, the electron mobility, and the effective mass at the same time as the doping level and the defect level are affected simultaneously. This demonstrates that relying on only one probe to characterize individual samples will prove futile in

many systems and that one needs to carry out measurements with significant statistics for robust information on doped graphene samples.

To compare the structural analysis by Raman spectroscopy to the electronic properties and further elucidate the types of scattering present in the samples, we measured the magnetoresistance (MR) in a cryostat at 3 K in a perpendicular magnetic field of up to B=8 T. The MR is determined from the sheet resistance $R_S(B)$

$$MR(B) = \frac{R_S(B) - R_S(0)}{R_S(0)}. \quad (0)$$

The results for sample A and B are shown in Fig. 3 together with the curve for the co-doped sample measured furthest away from the Dirac point. The other MR curves of the co-doped samples, which were shifted closer to the Dirac point by electrical gating, are shown in the supplementary information. All measurements were performed sufficiently far away from the Dirac point (between -4 and -10 x 10^{12} cm^{-1}) so that the variation of MR with charge carrier density becomes negligible. Comparing the three curves in Fig. 3, all of them show a local maximum of the resistance at zero magnetic field due to weak localization. At high fields the trends are very different (Fig. 3 inset). For the two N doped samples, A and B, the MR stays negative, going down monotonically for sample B and flattening for sample A. For the co-doped sample, we observe a sign change at around B = 4 T. As shown by McCann et al. [22], a positive high field MR can be associated to a scenario where the scattering is dominated by intervalley scattering induced by short range defects. In contrast the negative high field MR can be understood in terms of intravalley scattering dominated by long range charged impurities. Thus, the data would imply that the co-doped sample leads to effectively charge neutral defects while the N doped samples feature extended charged impurities while all the while the overall disorder remains comparable as indicated by the Raman measurements.

This is further supported as the co-doped sample shows the highest MR indicating low doping [23,24] while the negative MR values for samples A and B indicate higher doping. The nitrogen-doping as measured on sample A by XPS is 1.0% ± 0.1%. This finding is also in line with the values of the charge carrier mobility, which is expected to be higher for higher quality graphene. Comparing the three samples, the highest value is found for the co-doped sample. The lowest value is found for the nitrogen-doped sample B. These values are measured in a Hall-geometry (in a cryostat at 3 K), where we used [23]

$$\frac{R_H}{R_S} = B\mu \tag{2}$$

with R_H and R_S the Hall- and sheet resistance, the magnetic field B and the charge carrier mobility μ .

These results lead to an apparent contradiction with the co-doped sample showing a high MR and mobility, typically associated with pristine graphene [13,24], while at the same time showing the largest intensities for the defect induced Raman D peak. This can be resolved by distinguishing defects, or localized neutral impurities, from dopants, which act as charged long range scattering regions. In case of purely N doping the number of defects and dopants is equivalent, while having both nitrogen and boron atoms these dopants partially compensate. They all contribute as short-range localized defects enhancing the D peak intensity in the Raman measurement. However, the resulting small effective doping and thus an effectively small number of charged long range dopants will enhance the MR.

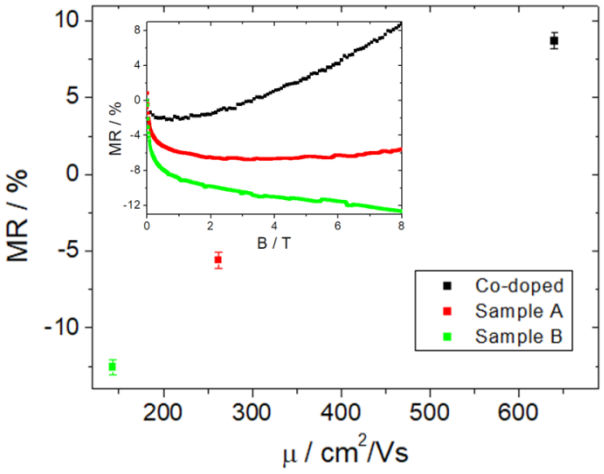

Figure 3: Comparison of the magnetoresistance at 8 T and the charge carrier mobility extracted from Hall-measurements. Inset: MR from 0 to 8 T for all three samples.

This qualitative discussion is further supported by a more quantitative analysis in terms of the electron scattering times. For the co-doped sample, MR measurements at different charge carrier densities were performed by applying gate voltages (Fig. SI1). They are all used within the quantitative analysis in this section. To extract the various scattering times, we fit the magnetoresistance for fields up to 0.3 T with a model that considers the phase coherence time τ_ϕ, the intervalley scattering time τ_i and the intravalley scattering $\tau_¿$ [22]:

$$\Delta R(B) = \frac{-e^2\rho_s^2}{\pi h}\left[F(dB\tau_\phi) - F\left(\frac{dB}{\tau_\phi^{-1}+2\tau_i^{-1}}\right) - 2F\left(\frac{dB}{\tau_\phi^{-1}+\tau_i^{-1}+\tau_¿^{-1}}\right)\right] \quad (3)$$

with $d=(4eD/\hbar)$, D the diffusion constant, $F(z)=\ln(z)+\Psi(1/2+1/z)$ and $\Psi(z)$ the digamma function. Here, we calculated the intravalley scattering according to Moser et al. [25] directly to reduce the number of free parameters. The resulting intravalley scattering times are summarized in Table 1 and support the interpretation introduced above as the scattering times for the co-doped samples are roughly a factor of two larger than for the Nitrogen-doped samples, A and B. This again indicates the rather weak intravalley scattering for the co-doped samples with predominantly short-range scatterers.

Sample	A	B	Co	Co	Co	Co
Charge carrier density [10^{12} cm^{-2}]	-9.32	-5.7	-6.5	-5.7	-5.0	-4.4
Intravalley scattering time [10^{-15}s]	9.34	3.99	18.9	18.2	16.9	15.7

Table 1: The intravalley relaxation times as calculated from the electron mobility and the charge density according to Ref. 13. Errors as determined from the fit described therein are 0.1% for the charger carrier density and 1% for the intravalleyscattering time. The Fermi velocity used is v_F=1x10^6 m/s.

From the fitting, we find the corresponding intervalley scattering and phase coherence times as shown in Fig. 4. The intervalley scattering times for the N-doped samples are comparable, sample B, or smaller, sample A than those for the co-doped sample, which does not allow for an easy conclusion. However, the phase coherence time, an indicator for the existence of effective inelastic scattering is significantly larger for the co-doped samples. This points to stronger inelastic scattering for the N-doped samples which is indicative of a stronger scattering from charged, long range, perturbations in the N-doped in comparison to the co-doped samples.

Our results show that a complex interplay of intervalley and intravalley scattering caused by predominantly short-ranged defects and long-ranged dopants complicates simple predictions for co-doped samples. The theoretical predictions of band gap engineering in slightly artificial co-doped systems where the dopants form dimers [26] or specific configurations around DV(555-777) defects[27] are probably unrealistic in real life devices where defect formation and sample preparations are much more complex.

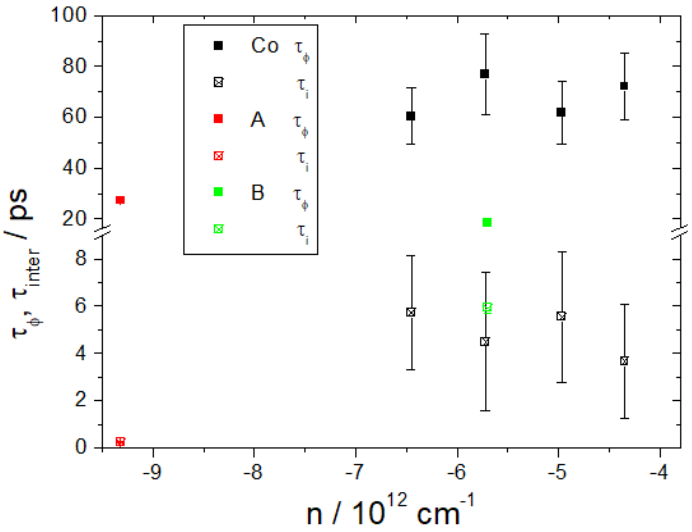

Figure 4: Phase coherence time and intervalley scattering time as extracted from the MR curve. For the co-doped samples different charge carrier densities were obtained by applying a gate voltage.

Furthermore, ensuring the homogeneity of such properties of reasonably large structures becomes an even more difficult challenge. Our works show that standard procedures lead to sizable inhomogeneities across the samples with randomly placed B and N defects partially compensating the degree of doping and in turn leading to more short-range defects in contrast to the long-ranged dopants in standard N-doped samples.

With that in mind we will explore a further method to exploit possible functionalities in differently doped graphene sheets by combining them. In the following, we discuss initial results for junctions prepared from differently doped graphene sheets brought into direct electronic contact via a region of twisted bi-layer graphene.

Lateral joining of differently doped graphene sheets

The lateral joining of areas with different doping type is well known from semiconductor physics leading to applications such as diodes and classical transistors [28,29]. To generate such a configuration using

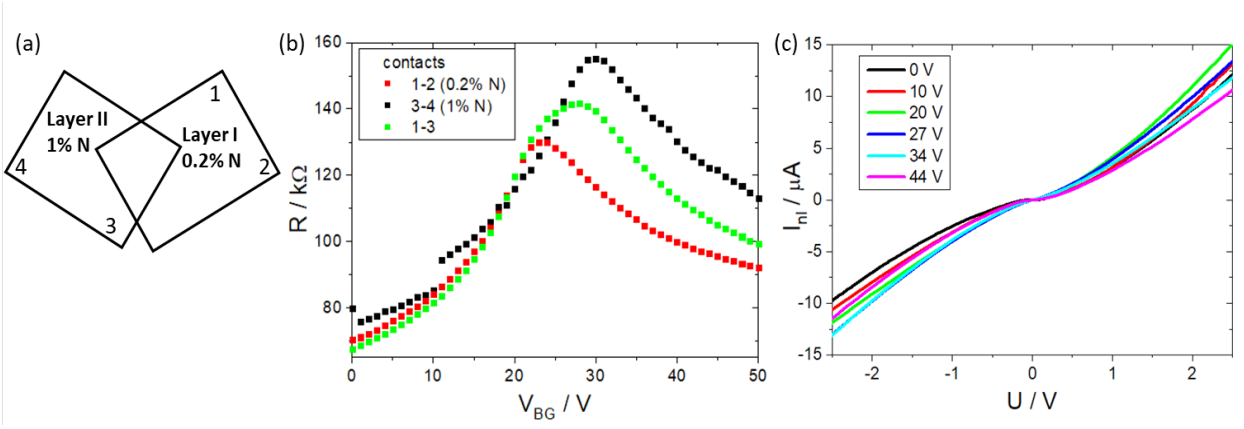

Figure 5: (a) Sketch of the sample. Layer I with 0.2% N is deposited and layer II with 1% N is deposited on top. For details see Methods. (b) Gate curves measured on different parts of the sample; contacts as depicted in (a). (c) The non-linear part of the IV curves between contacts 1-3 for different gate voltages. 27 V corresponds to an intermediary state between the charge neutrality points of the individual layers.

graphene, we deposited differently doped graphene sheets on top of each other. Their respective doping level with nitrogen is 0.2% for layer I and 1% for layer II and they are partly overlapping as sketched in Fig 5a. A microscope image of the different steps of the double transfer can be seen in Fig 6.

The sample was contacted via 4 silverpaste contacts, two on each layer. Measuring the gate dependence of the resistance (Fig. 4b), the charge neutrality point (CNP) is visible for the two layers with distinct levels of doping and changes depending on the doping from 23.5 V for 0.2% nitrogen to 30 V for 1%

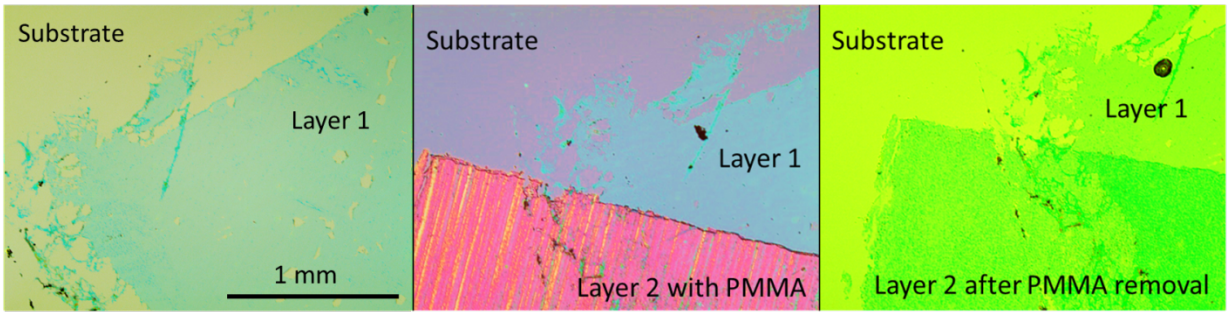

Figure 6: Microscope image of the different steps of the double transfer: First layer 1 is transferred and the PMMA removed (left image). The next layer is transferred with PMMA still present (middle image). The PMMA is removed with acetone (right image).

nitrogen. Overall, the CNP is placed at positive gate voltages due to adsorbed oxygen [30]. Measuring across the junction, the CNP is a superposition of the two individual layer peaks with a maximum in between and is slightly broadened. In the region between the two CNPs of 23.5 V and 30 V, layer I is in an n-doped state while layer II is in a p-doped state forming possibly a pn-junction. Measuring the IV-characteristics between contacts 1-3 an effective pn-junction ought to introduce stronger non-linear contributions. In Fig. 4c we present these non-linear contributions having removed the linear part as defined by the zero-field resistance depicted in Fig. 4b. In this representation, regions of horizontal IV characteristics indicate linear behavior and any deviation from this signifies non-linear contributions. From Fig. 4c it is clearly visible that this non-linear contribution becomes much more prominent in the region of gate voltages ranging from 20 V - 34 V which is precisely the region where we expect the effective pn junction to form. However, overall the effect is weak and to achieve a more pronounced pn-junction effect, it would be necessary to move the CNPs of the individual graphene layers further apart via more pronounced effects arising from doping. Presumably, this would require even more pure and clean pristine graphene flakes complicating the preparation of such junctions or nanopatterned devices where the junction forms a large part of the probed area.

As the cleanliness becomes a crucial factor for these junctions, we investigated the impact of the second transfer on the properties of the first layer in more detail via Raman spectroscopy (see Fig. 6). Both, the

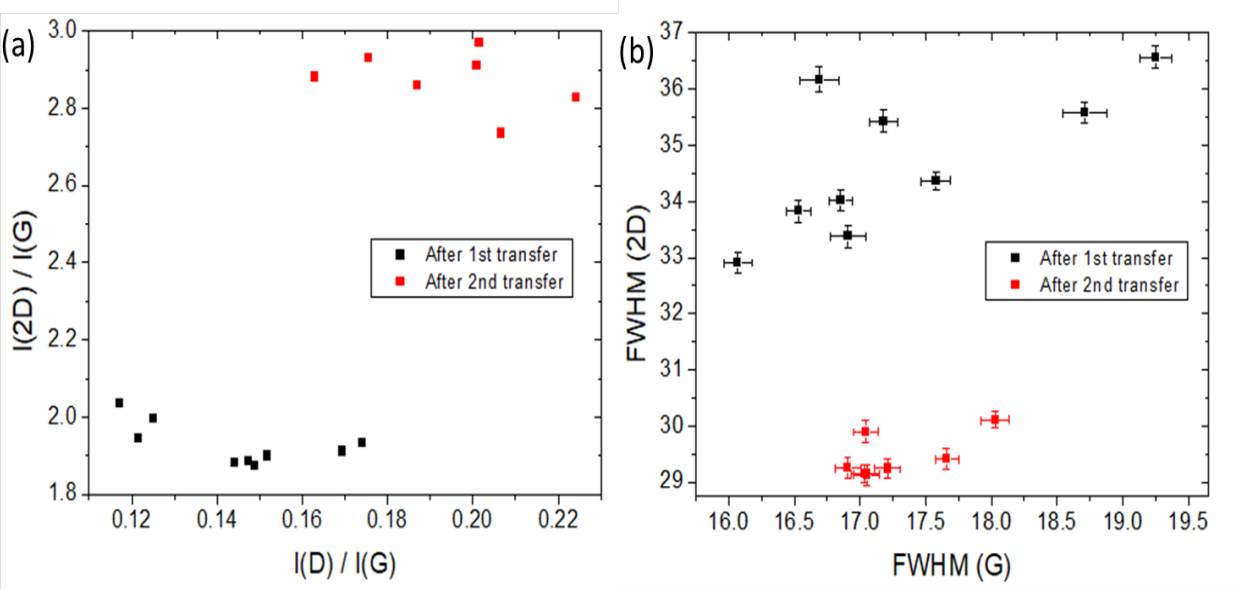

Figure 7: Comparison of the peak height of the 2D and D peaks as well as the FWHM of the 2D peaks from Raman spectroscopy for layer I before and after the second transfer. (a) Intensity of the 2D peak divided by that of the G peak as a function of the D peak intensity divided by that of the G-peak. (b) FWHM of the 2D peak as a functionpf that of the G peak.

intensity of the 2D peak as well as the intensity of the D peak is increased after the double transfer. While the increased 2D peak generally indicates more perfect graphene samples, the increased D peak is commonly associated with more defects [20]. However, as discussed above, the D peak intensity is not a monotonic function of the defect concentration, and it is hard to reach firm conclusion from the moderate change seen in Fig. 6 a. Furthermore, the sharp drop in the FWHM of the 2D peak after the transfer would point to less defects in line with the increase in the 2D intensity. This could be explained by adsorbates being removed during a second acetone bath and / or the subsequent heating. Fabricating a pn-junction via the presented transfer mechanism must take into account the impact of this procedure on the first layer. While the sample retains the basic graphene properties as shown here, the configuration of adsorbates or other defects may change considerably.

Summary

Using Raman spectroscopy and magneto-transport measurements we explored the structural and electronic properties of functionalized graphene addressing the effects of co-doping with B and N impurities. Our findings highlight the complexity of the induced changes for the electronic properties of graphene-based devices. While dopants such as B and N separately will introduce charged long-range scatterers the combination of both lead to effective charge neutral and short-range scattering centers affecting the magneto-transport properties. Accordingly, we find an enhancement of the intravalley scattering time via co-doping as well as an increase of the phase coherence time, both pointing to more short-ranged and charge-neutral defects. The main findings of the Raman spectroscopy highlight the significant inhomogeneities across individual samples. This points to the importance of a careful analysis of any Raman data as any individual measurement could point to different conclusions. As such this analysis enforces the requirement to probe a variety of distinct lateral positions in the Raman spectroscopy via even an averaging approach might be misleading.

A similar finding is shown for the lateral joining of differently doped graphene sheets in an effective p-n junction, where the Raman spectroscopy highlights the induced changes during the preparation process. Characterizing the individual sheets will not trivially translate into the understanding of the finally realized device.

Supplementary Material

See supplementary material for more curves of the magnetoresistance at different charge carrier densities for the co-doped sample, an exemplary XPS spectrum for sample A and more details about the methods that were used.

Acknowledgements

M.-L.B thanks Hao Lu for XPS measurements and Amir Tavabi for TEM measurements. M.G. acknowledges the visiting professorship program of the Centre for Dynamics and Topology and Johannes Gutenberg-University Mainz. This work was financially supported by the DFG primarily through the Priority Program Graphene SPP 1459 (Grant No. 130170629), SFB TRR 173 Spin + X, Projects A01 and B02 (Grant No. 268565370), and the Forschunginitiative Rheinland-Pfalz through the Center for Dynamics and Topology (TopDyn).

Bibliography

[1] F. Joucken, L. Henrard, and J. Lagoute, Phys. Rev. Mater. **3**, 110301 (2019).
[2] Y. Wang, Y. Shao, D.W. Matson, J. Li, and Y. Lin, ACS Nano **4**, 1790 (2010).
[3] A.L.M. Reddy, A. Srivastava, S.R. Gowda, H. Gullapalli, M. Dubey, and P.M. Ajayan, ACS Nano **4**, 6337 (2010).
[4] Y. Wang, Y. Shen, Y. Zhou, Z. Xue, Z. Xi, and S. Zhu, ACS Appl. Mater. Interfaces **10**, 36202 (2018).
[5] L.S. Panchakarla, K.S. Subrahmanyam, S.K. Saha, A. Govindaraj, H.R. Krishnamurthy, U.V. Waghmare, and C.N.R. Rao, Adv. Mater. **21**, 4726 (2009).
[6] S. Ullah, Q. Shi, J. Zhou, X. Yang, H.Q. Ta, M. Hasan, N.M. Ahmad, L. Fu, A. Bachmatiuk, and M.H. Rümmeli, Adv. Mater. Interfaces **7**, 2000999 (2020).
[7] Z.-S. Wu, A. Winter, L. Chen, Y. Sun, A. Turchanin, X. Feng, and K. Müllen, Adv. Mater. **24**, 5130 (2012).
[8] M.S. Kim, S. Cho, S.H. Joo, J. Lee, S.K. Kwak, M.I. Kim, and J. Lee, ACS Nano **13**, 4312 (2019).
[9] R. Verma, I. Chakraborty, S. Chowdhury, M.M. Ghangrekar, and R. Balasubramanian, ACS Sustain. Chem. Eng. **8**, 16591 (2020).
[10] W. Ai, Z. Luo, J. Jiang, J. Zhu, Z. Du, Z. Fan, L. Xie, H. Zhang, W. Huang, and T. Yu, Adv. Mater. **26**, 6186 (2014).
[11] S. Ullah, A. Hussain, W. Syed, M.A. Saqlain, I. Ahmad, O. Leenaerts, and A. Karim, RSC Adv. **5**, 55762 (2015).
[12] Y. Ito, C. Christodoulou, M.V. Nardi, N. Koch, H. Sachdev, and K. Müllen, ACS Nano **8**, 3337 (2014).
[13] M.-L. Braatz, L. Veith, J. Köster, U. Kaiser, A. Binder, M. Gradhand, and M. Kläui, Phys. Rev. Mater. **5**, 084003 (2021).
[14] L.M. Malard, M.A. Pimenta, G. Dresselhaus, and M.S. Dresselhaus, Phys. Rep. **473**, 51 (2009).
[15] F. Tuinstra and J.L. Koenig, J. Chem. Phys. **53**, 1126 (1970).
[16] D. Graf, F. Molitor, K. Ensslin, C. Stampfer, A. Jungen, C. Hierold, and L. Wirtz, Nano Lett. **7**, 238 (2007).
[17] G.S. Papanai, I. Sharma, and B.K. Gupta, Mater. Today Commun. **22**, 100795 (2020).
[18] A. Eckmann, A. Felten, A. Mishchenko, L. Britnell, R. Krupke, K.S. Novoselov, and C. Casiraghi, Nano Lett 6 (2012).
[19] M. Bruna, A.K. Ott, M. Ijäs, D. Yoon, U. Sassi, and A.C. Ferrari, ACS Nano **8**, 7432 (2014).
[20] M.M. Lucchese, F. Stavale, E.H.M. Ferreira, C. Vilani, M.V.O. Moutinho, R.B. Capaz, C.A. Achete, and A. Jorio, Carbon **48**, 1592 (2010).
[21] S. Berciaud, S. Ryu, L.E. Brus, and T.F. Heinz, Nano Lett. **9**, 346 (2009).

[22] E. McCann, K. Kechedzhi, V.I. Fal'ko, H. Suzuura, T. Ando, and B.L. Altshuler, Phys. Rev. Lett. **97**, 146805 (2006).
[23] M. Rein, N. Richter, K. Parvez, X. Feng, H. Sachdev, M. Kläui, and K. Müllen, ACS Nano **9**, 1360 (2015).
[24] X. Li, J. Zhuang, Y. Sun, J. Bai, Z. Zafar, Z. Ni, B. Jin, and Z. Shi, Carbon **82**, 346 (2015).
[25] J. Moser, H. Tao, S. Roche, F. Alzina, C.M. Sotomayor Torres, and A. Bachtold, Phys. Rev. B **81**, 205445 (2010).
[26] M. Alattas and U. Schwingenschlögl, Sci. Rep. **8**, 17689 (2018).
[27] D. Sen, R. Thapa, and K.K. Chattopadhyay, ChemPhysChem **15**, 2542 (2014).
[28] M. Riordan and L. Hoddeson, IEEE Spectr. **34**, 46 (1997).
[29] J. Wang, Z. Li, H. Chen, G. Deng, and X. Niu, Nano-Micro Lett. **11**, 48 (2019).
[30] H.I. Wang, M.-L. Braatz, N. Richter, K.-J. Tielrooij, Z. Mics, H. Lu, N.-E. Weber, K. Müllen, D. Turchinovich, M. Kläui, and M. Bonn, J. Phys. Chem. C **121**, 4083 (2017).